Supplementary Material

Seismic Energy Partitioning Across the Continuum of Laboratory Fault Slip Modes

Federico Pignalberi*[1,2], Giacomo Mastella[1], Carolina Giorgetti[1,3], Chris Marone[1,4], and Marco Maria Scuderi[1]

[1]***Dipartimento di Scienze della Terra, Sapienza Università di Roma, Rome, Italy***

[2]***Department of Engineering Geology and Hydrogeology, RWTH-Aachen University, Aachen, Germany***

[3]***Laboratoire de Géologie, École Normale Supérieure-PSL, CNRS PSL Research University, Paris, France***

[4]***Department of Geosciences, Pennsylvania State University, PA, USA***

This Supplementary Material provides additional figures and extended analyses supporting the results presented in the main text. It includes representative acoustic emission waveforms and source displacement spectra (Supplementary Figures 1–3), a compilation of breakdown work and seismic moment scaling across laboratory, mining-induced, and natural seismicity (Supplementary Figure 4), and characterizations of fault slip dynamics as a function of recurrence time, friction drop, and loading stiffness (Supplementary Figures 5–6). Post-experiment microstructural observations are presented in Supplementary Figure 7. Estimator comparison and robustness analyses for all power-law scaling relations discussed in the main text are reported in Supplementary Figures 8–11. Additional analyses include the evolution of seismic and aseismic event fractions with seismic moment (Supplementary Figure 12), slip duration and temporal seismic efficiency scaling (Supplementary Figure 13), per-experiment breakdown work scaling (Supplementary Figure 14), shear stress trajectories grouped by slip size class and stiffness configuration (Supplementary Figures 15–16), stationarity of peak shear stress across stiffness conditions (Supplementary Figure 17), and the temporal evolution of acoustic emission swarms relative to fault failure for slow and fast slip events (Supplementary Figures 18–19).

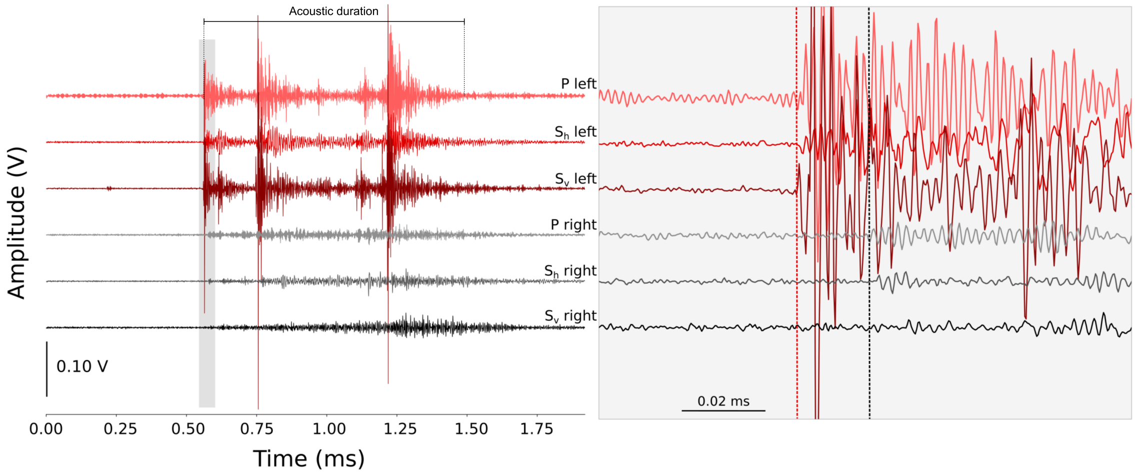

Supplementary Figure 1: Example waveforms showing acoustic emissions from a slip event. Top three traces (light red, red, dark red) are from sensors on the left side of the sample, bottom three (light gray, gray, black) are from the right side. P, Sh and Sv denote P-wave sensor (perpendicularly oriented) and horizontally/vertically polarized S-wave sensors respectively. Earlier arrival times and higher amplitudes on the left sensors indicate the seismic source originated in the left gouge layer. Right panel shows a zoomed view of the P-wave arrivals, with the red dashed lines marking the arrival times on the left side and black dashed line marking the arrival time on the right side block.

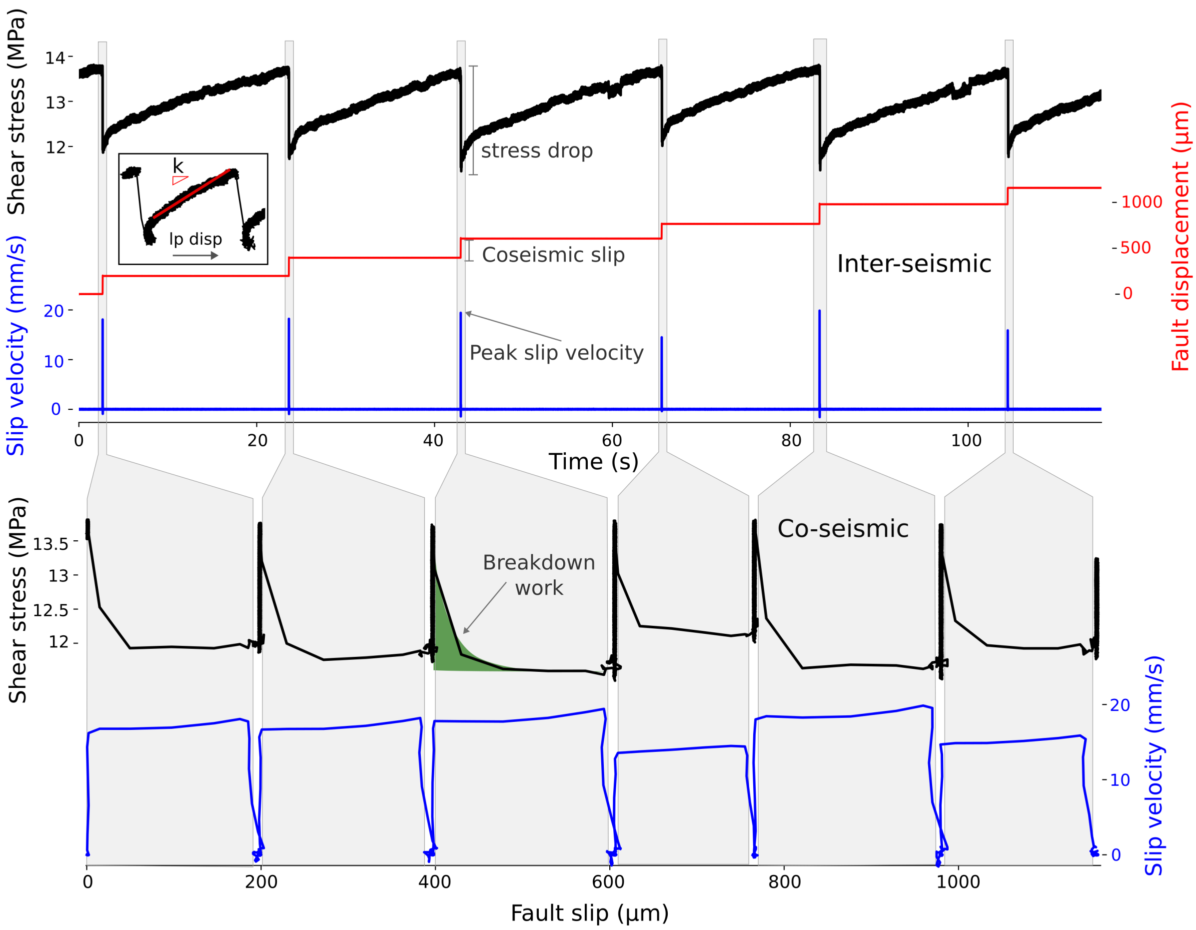

Supplementary Figure 2: Multiple stick-slip cycles. The upper panel shows the time series of shear stress (black line), fault displacement (red line), and slip velocity (blue line). The inset illustrates the shear stress as a function of the load point displacement and highlights the stiffness of the loading phase with the red line. The gray areas represent the co-seismic phase while the white areas the inter-seismic phase. The lower panel presents the same data plotted against fault slip. A representative breakdown work calculation is shown by the green shaded area for one event. Peak slip velocities are reached during the co-seismic phase, while periods of negligible slip velocity correspond to inter-seismic phases. Key features labeled include the stress drop, co-seismic slip, peak slip velocity, stiffness and breakdown work.

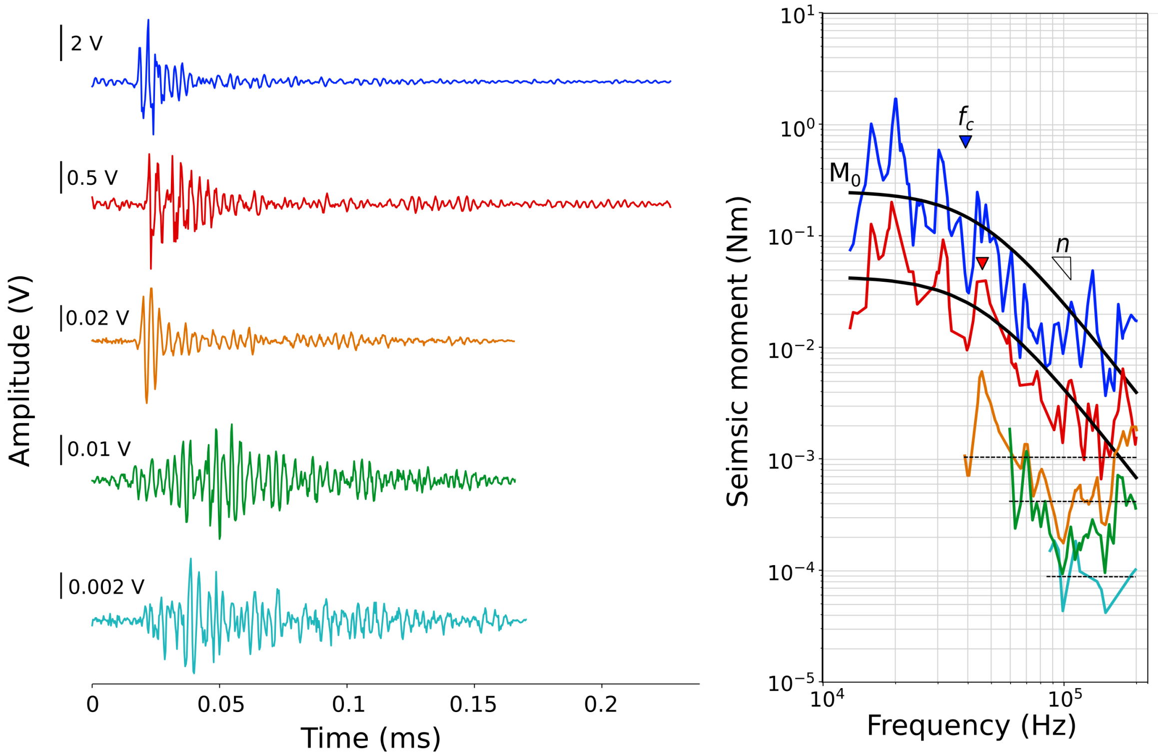

Supplementary Figure 3: (a) Acoustic emission waveforms with different amplitudes, arranged from strongest (top) to weakest (bottom). (b) Corresponding source displacement spectra with omega-square model fits (black solid lines). The black dashed lines represent the seismic moment (M_0) level for the smaller acoustic emissions. The spectral parameters are indicated: seismic moment (M_0), high-frequency decay (n), and corner frequency (f_c) indicated with a triangle.

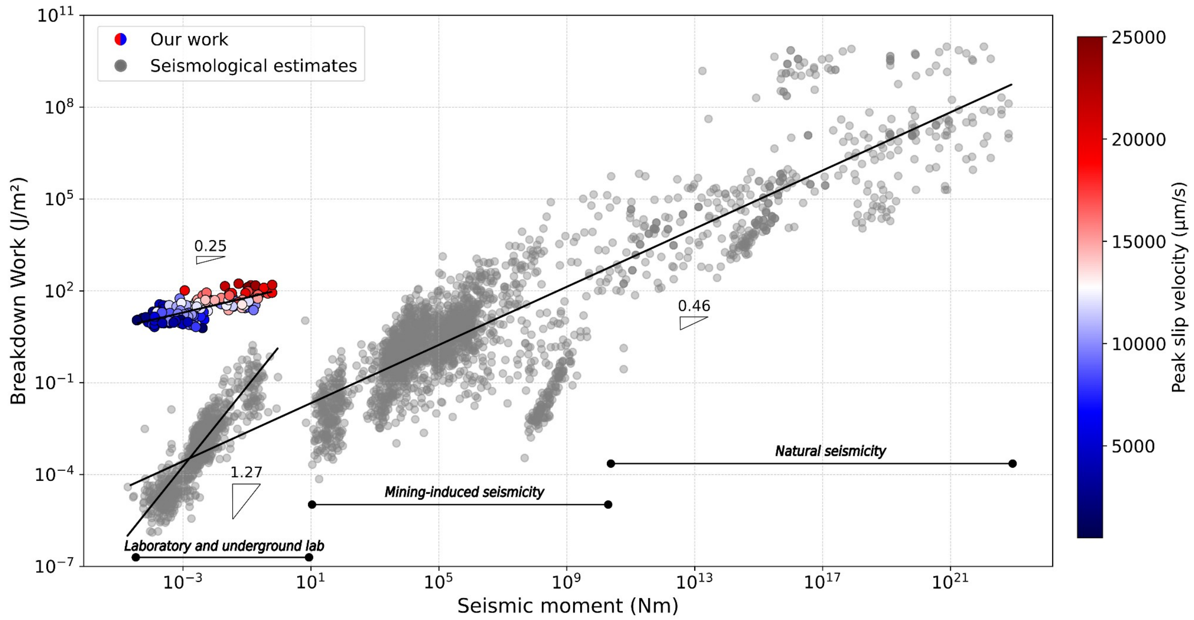

Supplementary Figure 4: Relationship between breakdown work and seismic moment seismologically derived. The dataset from (Aretusini et al., [2022]) includes laboratory and underground seismicity, mining induced seismicity and natural seismicity that refers to: laboratory events (Collins and Young, [2000]; Goodfellow and Young, [2014]; G. C. McLaskey, B. D. Kilgore, et al., [2014]; Sellers et al., [2003]; Yoshimitsu et al., [2014]; P. A. Selvadurai, [2019]), mine-induced seismicity (Gibowicz et al., [1991]; Kwiatek, Plenkers, et al., [2011]; Oye et al., [2005]; Spottiswoode and McGarr, [1975]; Urbancic, Trifu, and Young, [1993]; Urbancic and Trifu, [1996]), and natural earthquakes (Abercrombie and J. Rice, [2005]; Baltay, Ide, et al., [2011]; Ide, G. C. Beroza, et al., [2003]; Imanishi and Ellsworth, [2013]; Mori et al., [2003]; J. R. Rice, [2006]; Viesca and Garagash, [2015]).

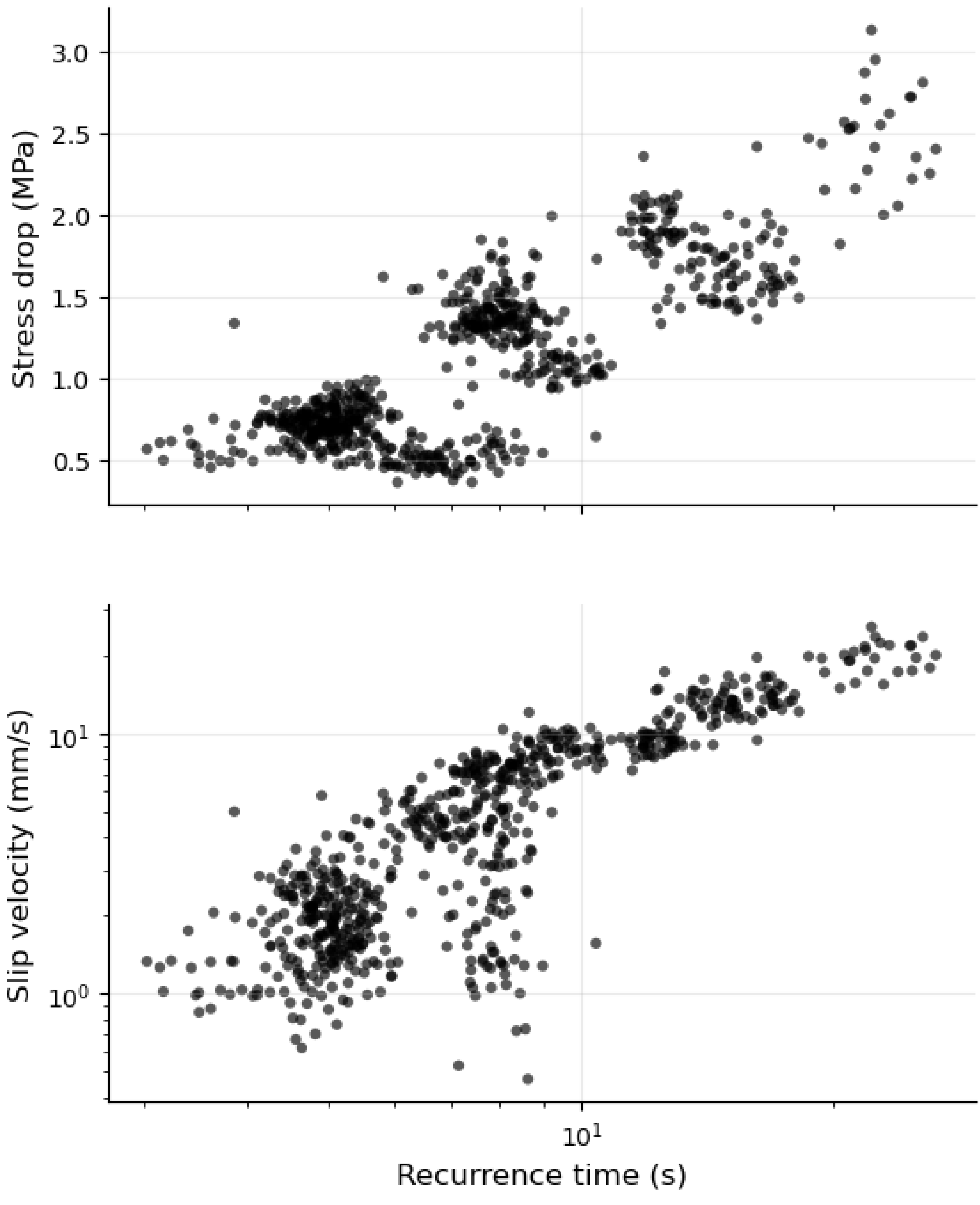

Supplementary Figure 5: Stress drop and peak slip velocity as a function of inter-event recurrence time. (**a**) Stress drop (MPa) versus recurrence time (s) and (**b**) peak slip velocity (mm/s) versus recurrence time (s), both on semi-logarithmic axes. Each dot represents an individual slip event from all experiments. Both stress drop and peak slip velocity increase systematically with recurrence time, forming distinct clusters that reflect the different stiffness configurations. Events with short recurrence intervals ($\lesssim$ 5 s) cluster at low stress drops ($\sim$ 0.5–1.0 MPa) and low slip velocities ($\sim$ 1–2 mm/s), characteristic of slow slip under high stiffness conditions ($k/k_c \gtrsim 1$). Events with longer recurrence times ($\gtrsim$ 10 s) show progressively larger stress drops ($\sim$ 1.5–3.0 MPa) and higher peak slip velocities ($\gtrsim$ 10 mm/s), consistent with fast, dynamic rupture under low stiffness conditions ($k/k_c < 1$). This positive correlation between recurrence time and both stress drop and slip velocity is consistent with the interpretation that longer inter-event periods allow greater frictional restrengthening through asperity healing, resulting in larger stored elastic energy and more energetic ruptures upon failure.

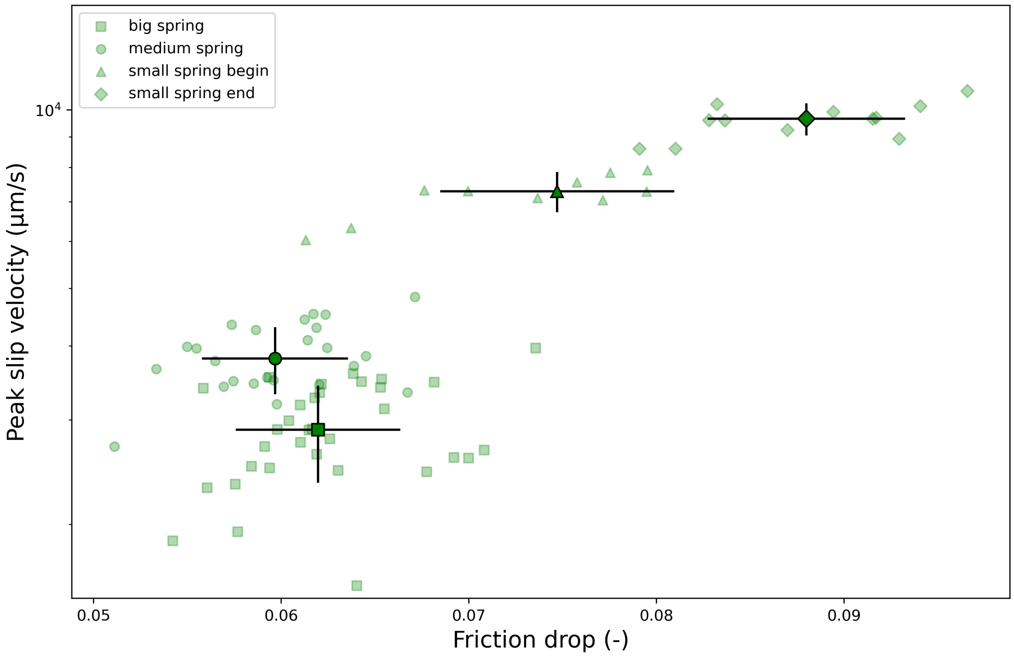

Supplementary Figure 6: Peak slip velocity increases with friction drop, confirming stiffness-controlled slip behavior. Scatter plot showing the relationship between friction drop and peak slip velocity for different loading stiffness conditions (big, medium, and small spring experiments). Error bars mark median values and their statistical variability. Both during the forward and reverse stiffness sequence, events under lower system stiffness (small-spring conditions) consistently exhibit larger friction drops and higher slip velocities, demonstrating a tendency toward unstable, dynamic rupture. Conversely, higher stiffness (big-spring) produces smaller friction drops and lower slip velocities, associated with more stable slip. This systematic trend confirms that stiffness is the primary control on the transition from stable/slow to unstable/fast fault slip.

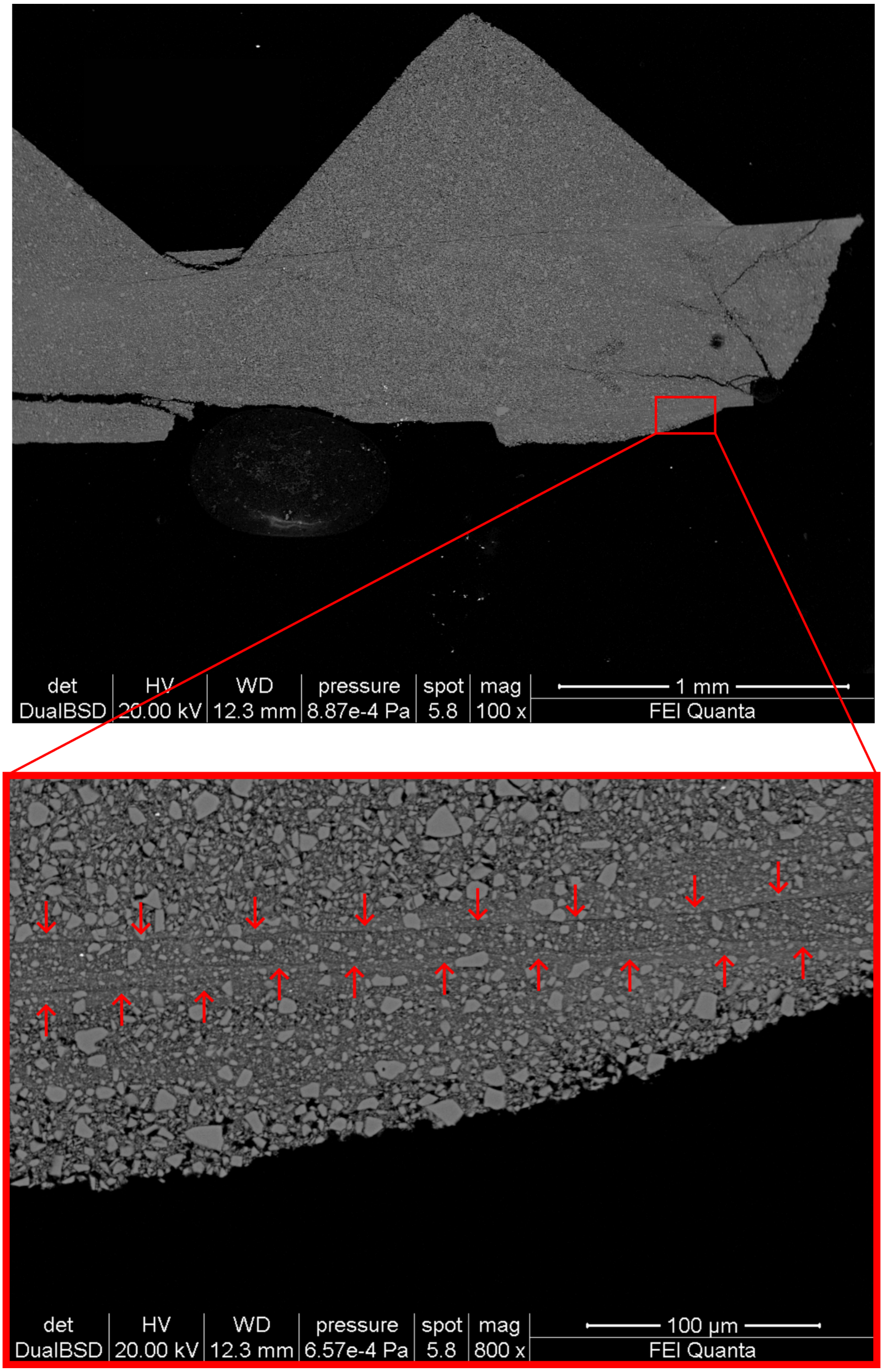

Supplementary Figure 7: Backscattered electron SEM images of the experimental fault zone after experiment s0109 (18 MPa normal stress). (a) Low-magnification view (100×) showing the entire gouge layer thickness. (b) High-magnification image (800×) of the area highlighted by the red box, revealing the development of a highly localized shear zone. Red arrows indicate the main slip surface where deformation is concentrated, characterized by grain size reduction and intense shearing.

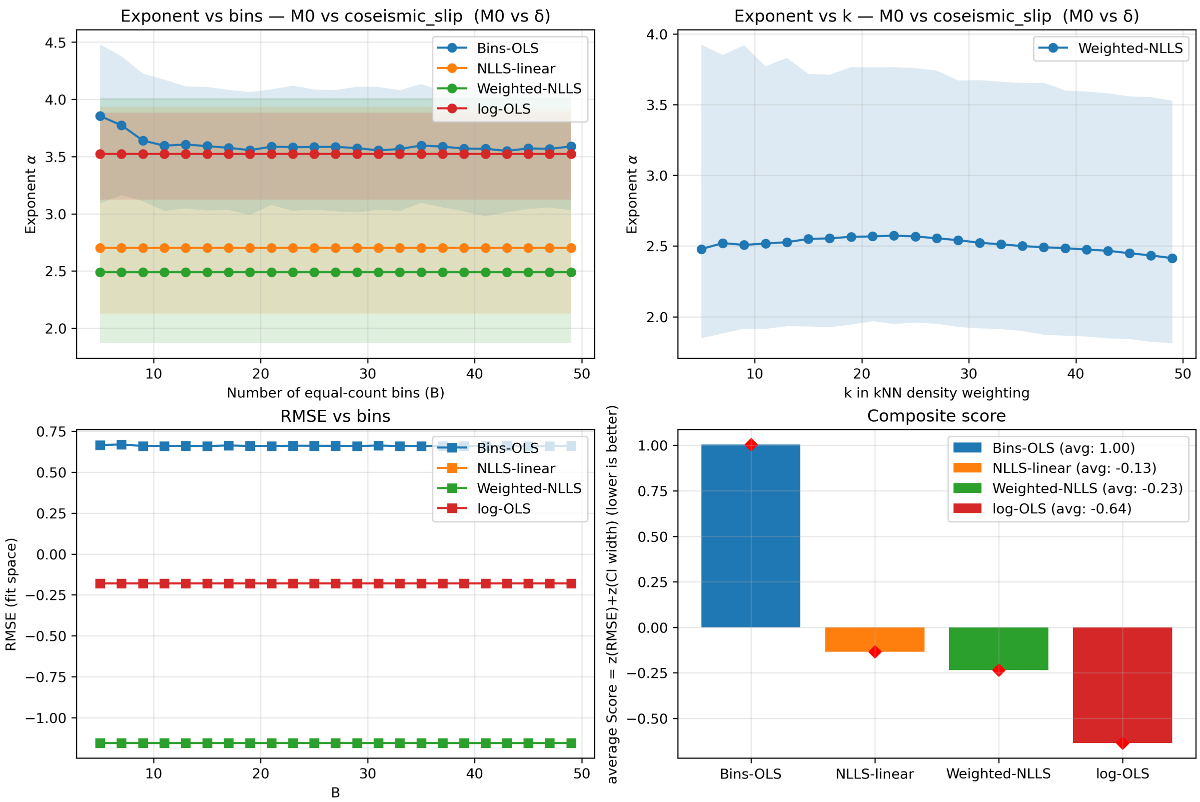

Supplementary Figure 8: Estimator comparison and robustness analysis for the M_0–δ scaling relation. (**a**) Scaling exponent α as a function of the number of equal-count bins ($B = 6$–50) for four estimators: Bins-OLS (blue), NLLS-linear (orange), Weighted-NLLS (green), and log-OLS (red). Shaded areas represent 95% bootstrap confidence intervals. Log-OLS yields a stable exponent $\alpha \approx 3.53$ across all values of B, while Bins-OLS converges toward the same value for $B \gtrsim 10$. NLLS-linear and Weighted-NLLS return lower exponents ($\alpha \approx 2.7$ and $\alpha \approx 2.5$, respectively), consistent with their different residual models. (**b**) Exponent α from Weighted-NLLS as a function of k in kNN density weighting ($k = 5$–50). The slope remains stable at $\alpha \approx 2.5$ across the full sweep, with increasing CI width at low k. (**c**) RMSE (in fit space) as a function of B for all estimators. Log-OLS achieves the lowest RMSE among log-space methods, while Weighted-NLLS yields the lowest overall RMSE in linear space, reflecting differences in native fit spaces. (**d**) Composite robustness score $S = z(\text{RMSE}) + z(\text{CI width})$ averaged across the hyper-parameter sweep for each estimator (red diamonds indicate the mean). Log-OLS achieves the lowest average score ($S = -0.64$), indicating the best joint performance in terms of residuals and slope uncertainty, and is therefore adopted as the primary estimator for the M_0–δ relation.

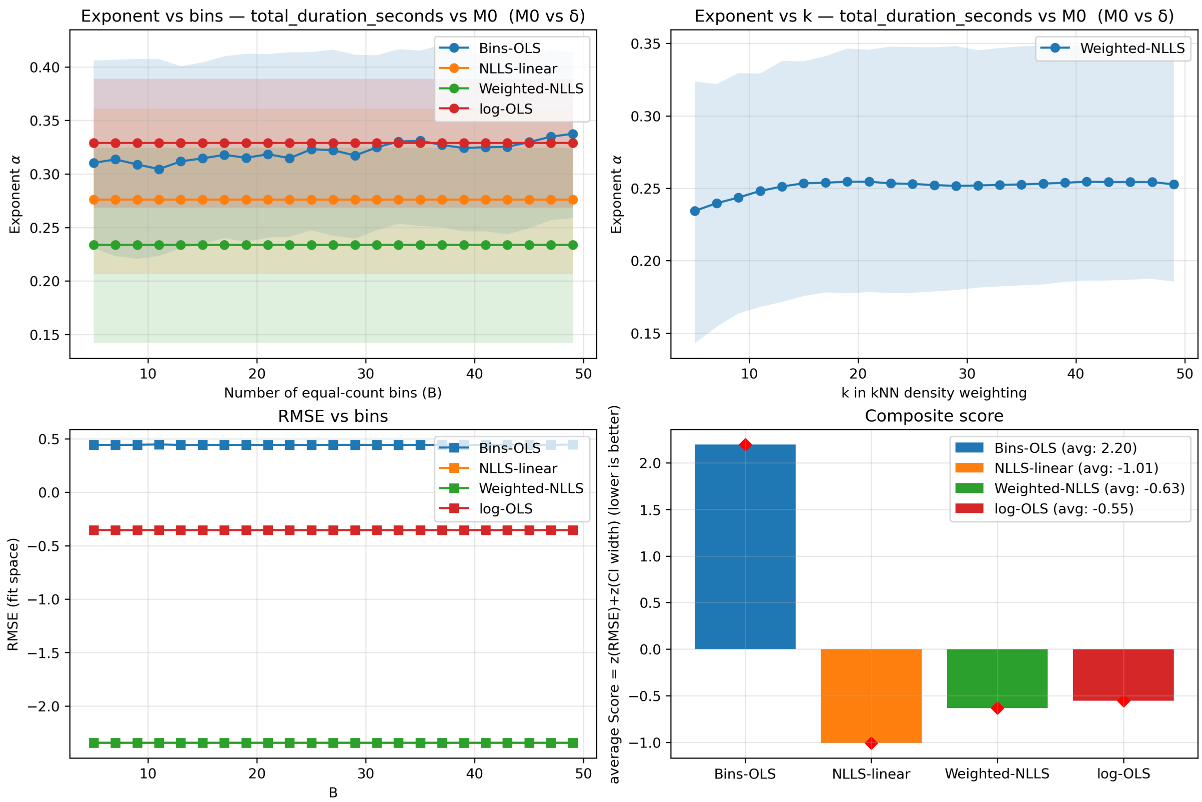

Supplementary Figure 9: Estimator comparison and robustness analysis for the total slip duration T_{total}–M_0 scaling relation. (**a**) Scaling exponent α as a function of the number of equal-count bins ($B = 6$–50) for four estimators: Bins-OLS (blue), NLLS-linear (orange), Weighted-NLLS (green), and log-OLS (red). Shaded areas represent 95% bootstrap confidence intervals. Log-OLS yields a stable exponent $\alpha \approx 0.33$ across all values of B, close to the theoretical prediction $T \propto M_0^{1/3}$. NLLS-linear returns $\alpha \approx 0.28$, while Weighted-NLLS yields the lowest estimate ($\alpha \approx 0.23$), consistent with their different residual models. Bins-OLS shows wider confidence intervals and mild sensitivity to B at low bin counts. (**b**) Exponent α from Weighted-NLLS as a function of k in kNN density weighting ($k = 5$–50). The slope stabilizes at $\alpha \approx 0.25$ for $k \gtrsim 15$, with large CI width at low k indicating sensitivity to local density estimation at sparse k. (**c**) RMSE (in fit space) as a function of B for all estimators. Weighted-NLLS achieves the lowest RMSE in linear space, while log-OLS performs best among log-space methods. (**d**) Composite robustness score $S = z(\text{RMSE}) + z(\text{CI width})$ averaged across the hyper-parameter sweep for each estimator (red diamonds indicate the mean). NLLS-linear achieves the lowest average score ($S = -1.01$), followed by Weighted-NLLS ($S = -0.63$) and log-OLS ($S = -0.55$), while Bins-OLS performs poorly ($S = 2.20$). NLLS-linear is therefore adopted as the preferred estimator for the T_{total}–M_0 relation, reflecting the additive noise structure of duration measurements.

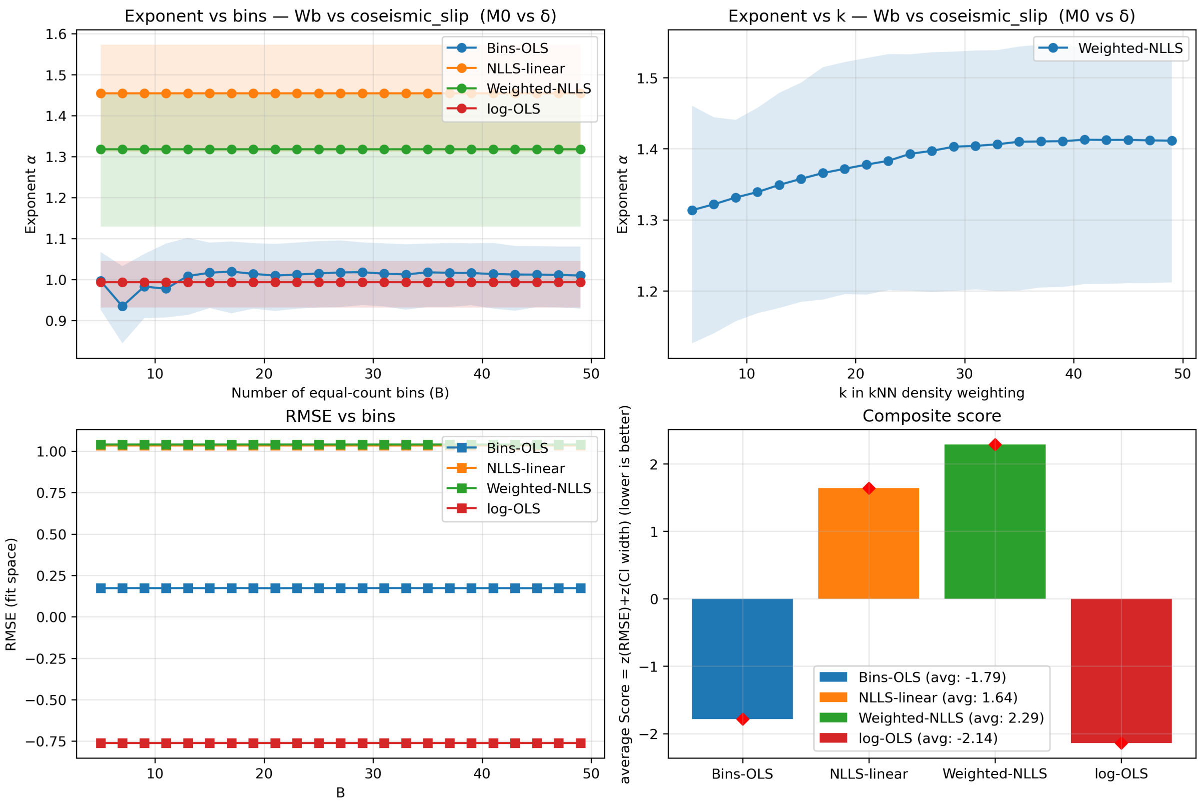

Supplementary Figure 10: Estimator comparison and robustness analysis for the W_b–δ scaling relation. (**a**) Scaling exponent α as a function of the number of equal-count bins (B = 6–50) for four estimators: Bins-OLS (blue), NLLS-linear (orange), Weighted-NLLS (green), and log-OLS (red). Shaded areas represent 95% bootstrap confidence intervals. Log-OLS and Bins-OLS converge to $\alpha \approx 1.0$, consistent with an approximately linear scaling $W_b \propto \delta$. NLLS-linear and Weighted-NLLS return systematically higher exponents ($\alpha \approx 1.45$ and $\alpha \approx 1.32$, respectively), reflecting their sensitivity to large-amplitude events under an additive residual model. (**b**) Exponent α from Weighted-NLLS as a function of k in kNN density weighting (k = 5–50). The slope increases monotonically from $\alpha \approx 1.31$ to $\alpha \approx 1.41$ with increasing k, indicating sensitivity to the density weighting at large k, and is therefore disfavored for this relation. (**c**) RMSE (in fit space) as a function of B for all estimators. Log-OLS achieves the lowest RMSE among all methods (RMSE ≈ -0.75), stable across all values of B, while Weighted-NLLS and NLLS-linear show significantly higher residuals in their respective fit spaces. (**d**) Composite robustness score $S = z(\text{RMSE}) + z(\text{CI width})$ averaged across the hyper-parameter sweep (red diamonds indicate the mean). Log-OLS achieves the lowest average score ($S = -2.14$), followed by Bins-OLS ($S = -1.79$), while NLLS-linear ($S = 1.64$) and Weighted-NLLS ($S = 2.29$) perform poorly. Log-OLS is therefore adopted as the primary estimator for the W_b–δ relation, with Bins-OLS as a decade-balanced corroboration.

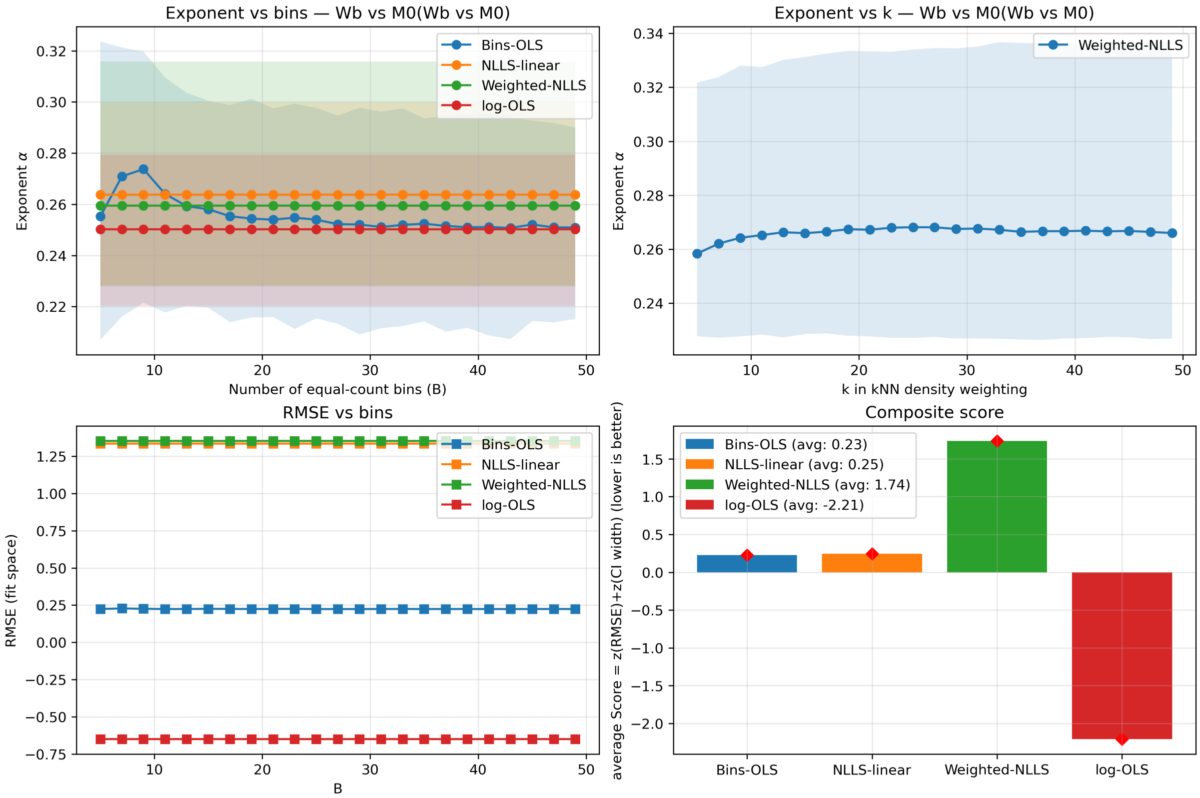

Supplementary Figure 11: Estimator comparison and robustness analysis for the W_b–M_0 scaling relation. (**a**) Scaling exponent α as a function of the number of equal-count bins ($B = 6$–50) for four estimators: Bins-OLS (blue), NLLS-linear (orange), Weighted-NLLS (green), and log-OLS (red). Shaded areas represent 95% bootstrap confidence intervals. All four estimators converge to a narrow range of sub-linear exponents ($\alpha \approx 0.25$–0.26), with log-OLS yielding the most stable estimate ($\alpha \approx 0.25$) and the tightest confidence interval across the full sweep. Bins-OLS shows mild sensitivity at low B ($B < 10$) before stabilizing at $\alpha \approx 0.26$ for larger bin counts. (**b**) Exponent α from Weighted-NLLS as a function of k in kNN density weighting ($k = 5$–50). The slope stabilizes rapidly at $\alpha \approx 0.26$–0.27 for $k \gtrsim 10$, with CI width narrowing consistently, indicating robust behavior across the kNN sweep for this relation. (**c**) RMSE (in fit space) as a function of B for all estimators. Log-OLS achieves the lowest RMSE ($\mathrm{RMSE} \approx -0.65$), stable across all values of B. Bins-OLS shows intermediate performance, while NLLS-linear and Weighted-NLLS yield the highest RMSE (≈ 1.30) in their native linear space, reflecting the large dynamic range of W_b and M_0. (**d**) Composite robustness score $S = z(\mathrm{RMSE}) + z(\mathrm{CI\ width})$ averaged across the hyper-parameter sweep (red diamonds indicate the mean). Log-OLS achieves by far the lowest average score ($S = -2.21$), while Bins-OLS ($S = 0.23$) and NLLS-linear ($S = 0.25$) perform comparably, and Weighted-NLLS performs worst ($S = 1.74$). Log-OLS is therefore adopted as the primary estimator for the W_b–M_0 relation, consistent with the multiplicative scatter structure of this scaling.

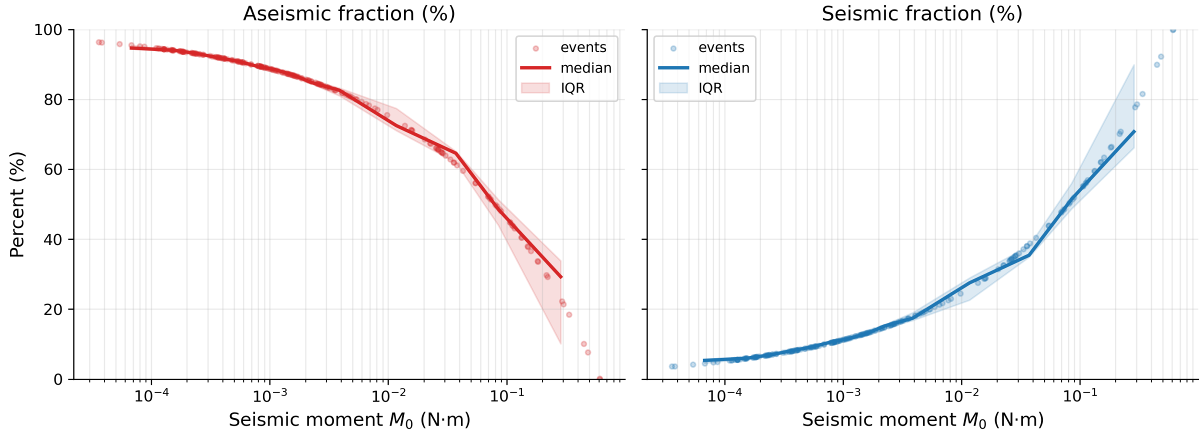

Supplementary Figure 12: Seismic and aseismic event fraction as a function of seismic moment. Fraction of aseismic (left) and seismic (right) events as a function of seismic moment M_0. Circles indicate individual events, solid lines represent the median trend obtained using equal-count binning in log-space, and shaded areas denote the interquartile range (IQR). The progressive shift from predominantly aseismic to predominantly seismic slip reflects the increasing contribution of brittle failure and acoustic energy release as slip becomes faster and larger.

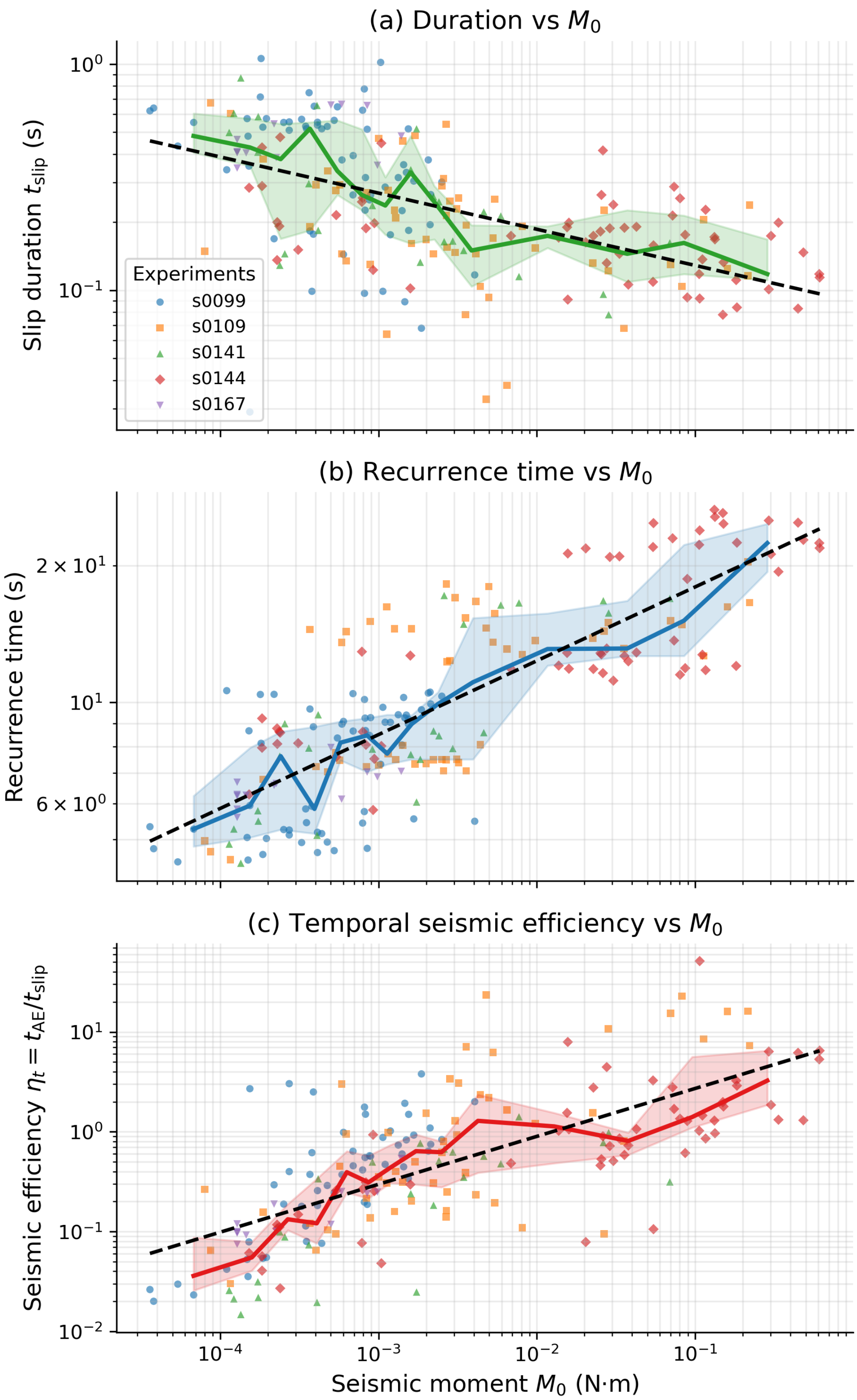

Supplementary Figure 13: Duration, recurrence time, and temporal seismic efficiency versus seismic moment. (a) Slip duration t_{slip} as a function of seismic moment M_0. (b) Recurrence time between consecutive slip events as a function of M_0. (c) Temporal seismic efficiency $\eta_t = t_{\text{ae}}/t_{\text{slip}}$ versus M_0. Colored markers represent individual events for the five experiments, the solid lines show the median obtained using equal-count binning in log-space, and shaded regions denote the interquartile range (IQR). Black dashed lines indicate best-fit power-law reference trends as discussed in the Supplementary Methods. Increasing M_0 corresponds to shorter slip durations, longer recurrence intervals, and enhanced proportion of high-frequency acoustic radiation.

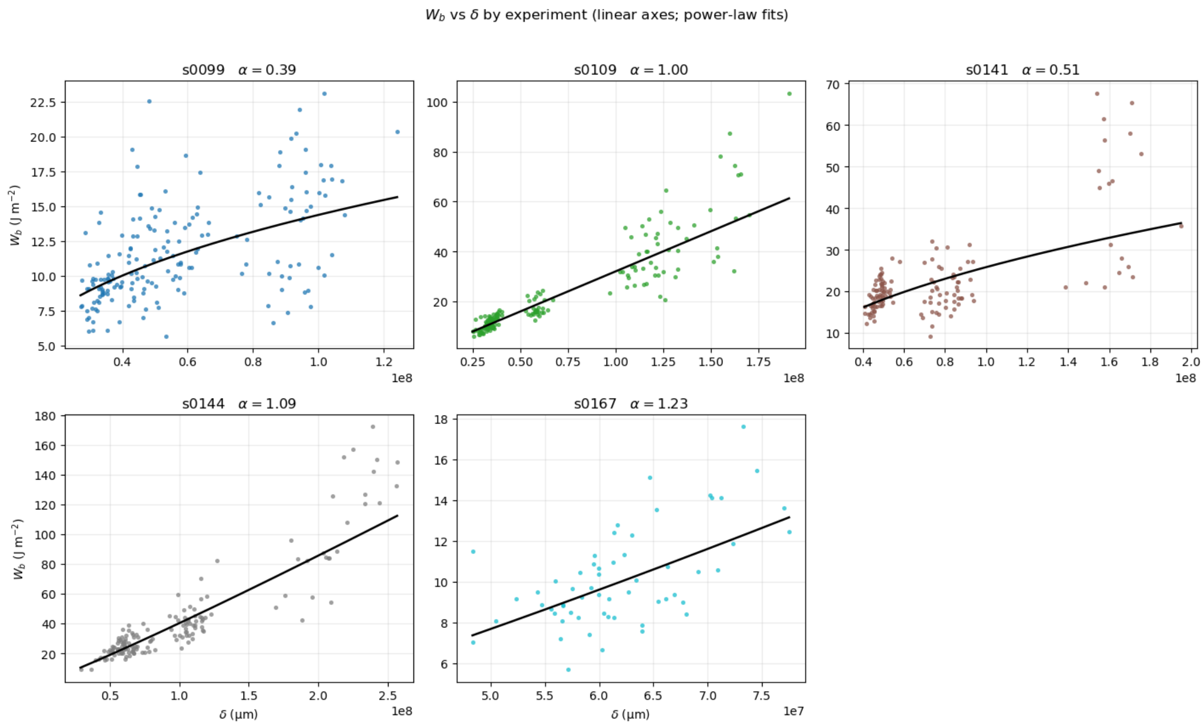

Supplementary Figure 14: Breakdown work W_b versus co-seismic slip δ for individual experiments, shown on linear axes with power-law fits (black solid lines). Each panel corresponds to one experiment (s0099, s0109, s0141, s0144, s0167), with the best-fit exponent α reported in the title. Individual events are shown as colored circles, with each experiment plotted in a distinct color. The fitted exponents range from $\alpha = 0.39$ (s0099, $\sigma_n = 11$ MPa) to $\alpha = 1.23$ (s0167, $\sigma_n = 8$ MPa), with a median close to unity, consistent with the global fit $W_b \propto \delta^{0.98}$ reported in the main text. The variability in α across experiments reflects differences in normal stress and stiffness conditions, which modulate the relative contributions of seismic and aseismic energy dissipation. Despite this scatter, all experiments show a positive, monotonically increasing trend of W_b with δ, confirming the robustness of the scaling across the full range of experimental conditions.

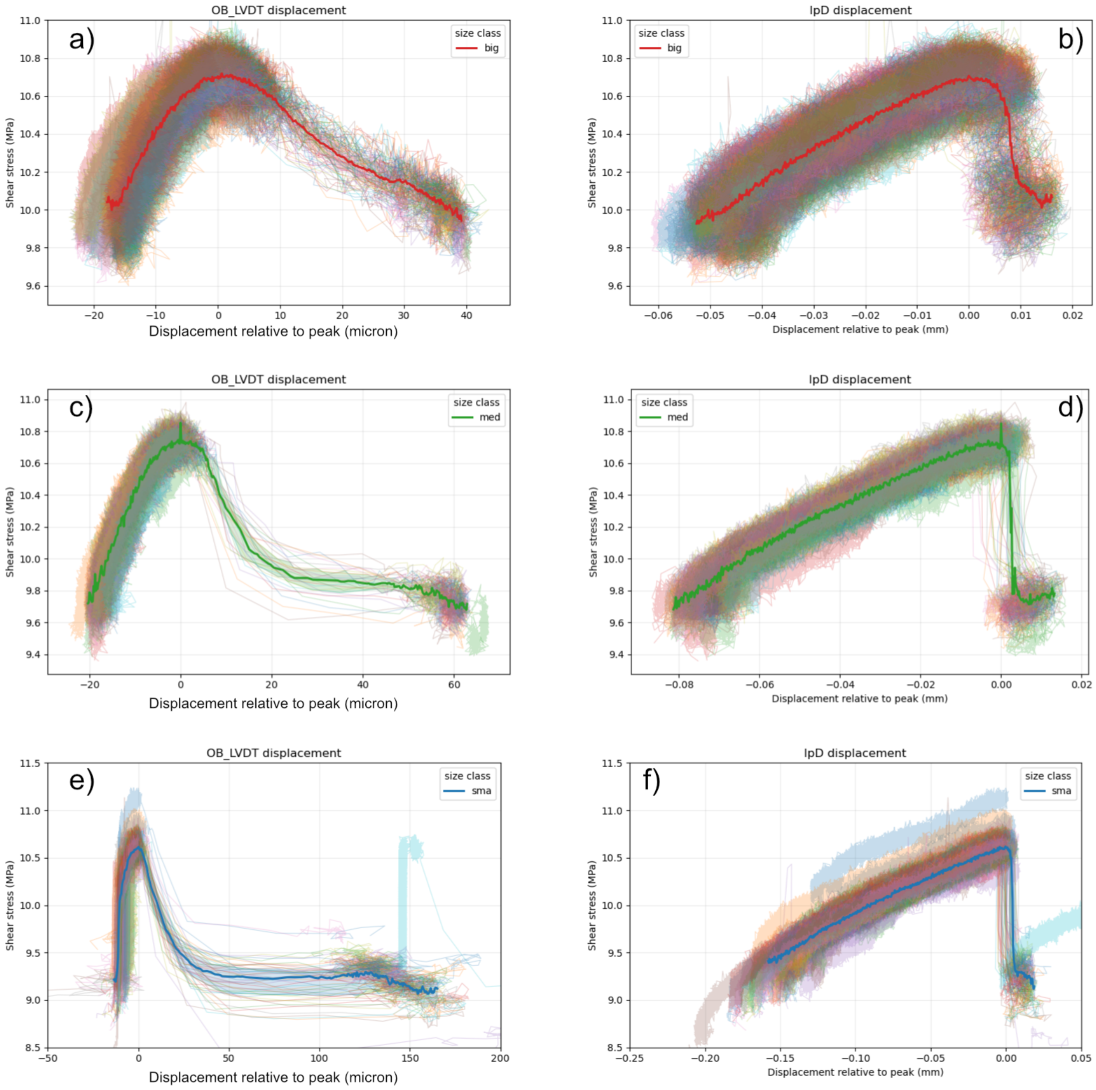

Supplementary Figure 15: Shear stress versus displacement relative to peak for all slip events, grouped by size class and shown for two displacement sensors: on-board LVDT (OB_LVDT, left column) and load point displacement (lpD, right column). Each thin line represents an individual event; the bold colored line shows the median trajectory for each size class. Events are classified into three size classes: large/fast (red, panels **a**–**b**), medium/slow (green, panels **c**–**d**), and small/slow (blue, panels **e**–**f**). The left column (OB_LVDT) captures fault-local displacement, while the right column (lpD) captures the displacement of the loading medium, highlighting the contrast between fault slip and elastic loading machine response. Large events (panels **a**–**b**) show a sharp, well-defined stress peak followed by an abrupt stress drop over a narrow displacement range, characteristic of fast, dynamic rupture. Medium events (panels **c**–**d**) display a broader, more gradual weakening phase, consistent with slow slip behavior. Small events (panels **e**–**f**) show highly variable trajectories with a diffuse stress peak and extended weakening, indicative of distributed, predominantly aseismic deformation. The systematic evolution from sharp to diffuse stress drop across size classes reflects the progressive transition from fast to slow slip governed by the stability ratio k/k_c.

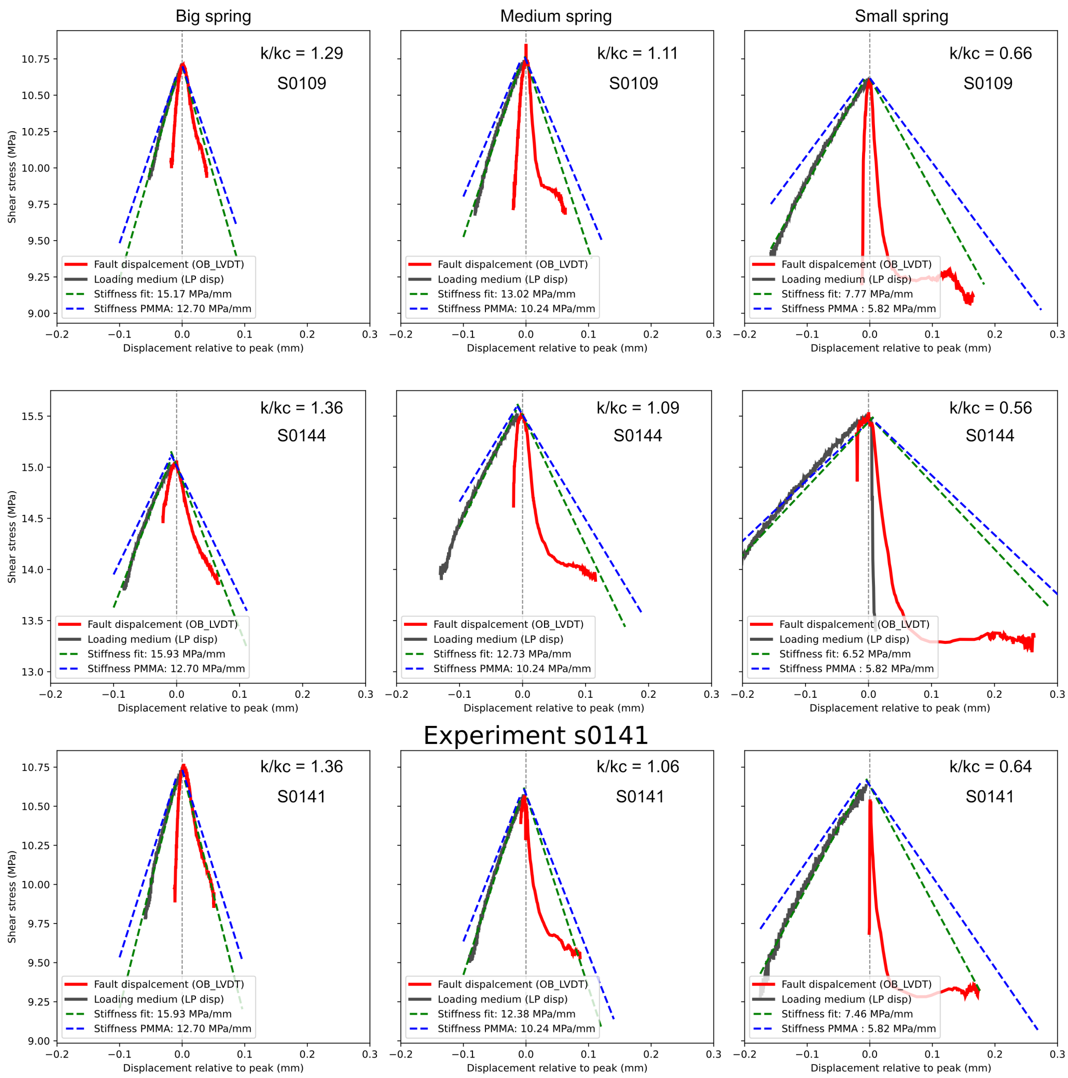

Supplementary Figure 16: Shear stress versus displacement relative to peak for representative slip events from three experiments (s0109, s0144, s0141, rows) and three loading stiffness configurations (big, medium, and small spring, columns), with the corresponding stability ratio k/k_c reported in each panel. Red curves show fault displacement measured by the on-board LVDT (OB_LVDT), while dark gray curves show the loading medium displacement (load point, LP disp). The green dashed line indicates the measured stiffness fit, and the blue dashed line shows the theoretical stiffness of the PMMA loading blocks for reference. As k/k_c decreases from left ($k/k_c > 1$, stable to slow slip) to right ($k/k_c < 1$, fast slip), the events transition from broad, gradual stress drops with extended weakening (big spring) to sharp, abrupt stress drops with large co-seismic displacement (small spring). The divergence between fault displacement (OB_LVDT) and load point displacement (LP disp) grows systematically with decreasing k/k_c, reflecting the increasing dynamic imbalance between elastic energy stored in the loading system and energy dissipated during rupture. The fitted stiffness values decrease progressively from big to small spring (∼15–16 MPa/mm to ∼6–8 MPa/mm), consistent with the nominal stiffness configurations $k_1 > k_2 > k_3$ described in the Methods.

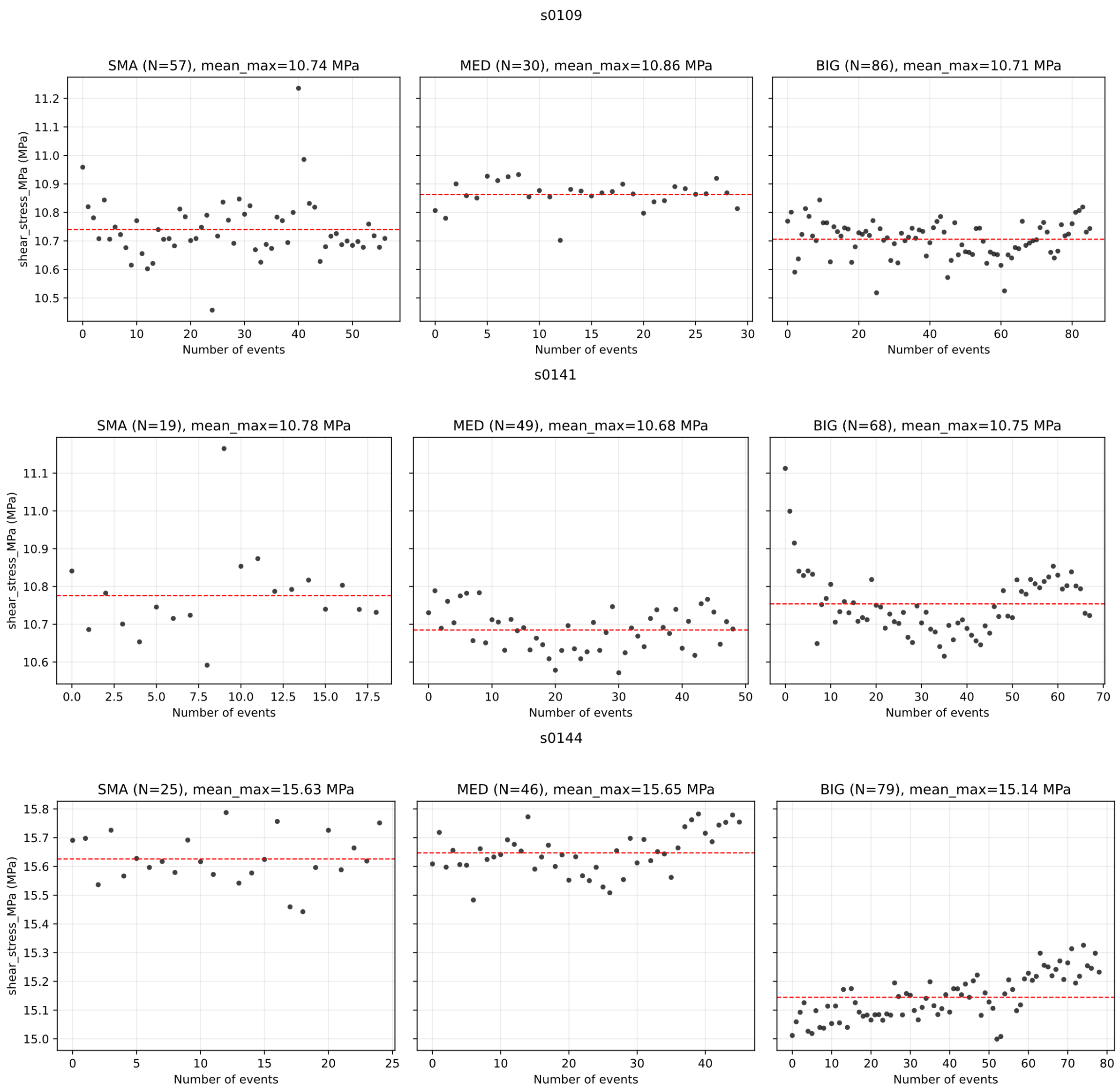

Supplementary Figure 17: Peak shear stress at failure as a function of event number for three experiments (s0109, s0141, s0144, rows) and three loading stiffness configurations (SMA: small spring, MED: medium spring, BIG: big spring, columns). Each black dot represents an individual slip event; the red dashed line indicates the mean peak shear stress for each configuration, with the number of events N and mean value reported in the panel title. Peak shear stress remains approximately stationary throughout each experiment, with no systematic trend as a function of event number, regardless of stiffness configuration or normal stress level. Mean values are remarkably consistent across stiffness configurations within each experiment (e.g., 10.71–10.86 MPa for s0109; 10.68–10.78 MPa for s0141; 15.14–15.65 MPa for s0144), confirming that the peak frictional strength at failure onset is effectively independent of loading stiffness. This observation supports the interpretation that the frictional constitutive properties and fault zone structure remain stationary across stiffness configurations within each experiment, and that the transition from slow to fast slip is governed by the elastodynamic stability ratio k/k_c rather than by changes in fault strength or cumulative shear strain.

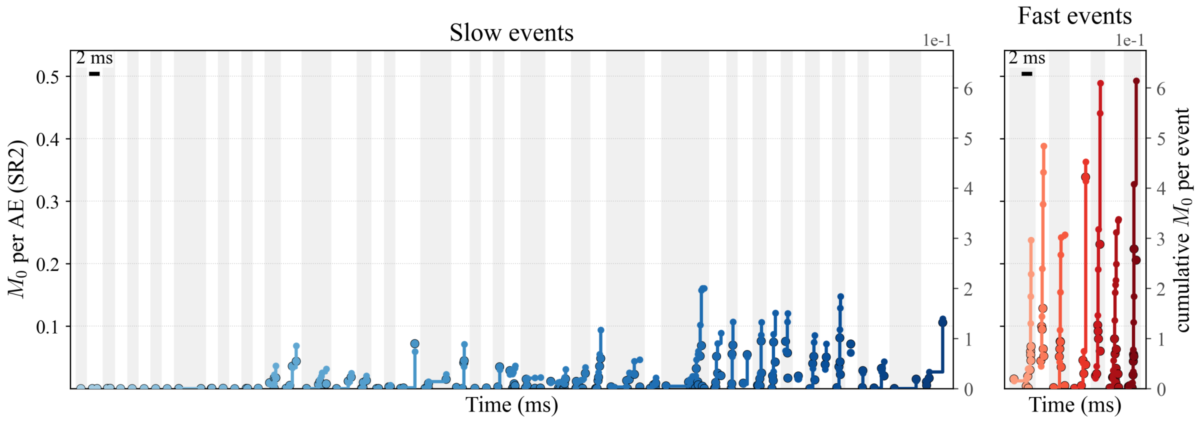

Supplementary Figure 18: Acoustic emission swarms versus isolated bursts in a representative experiment (s0144). Comparison of AE M_0 (left axis) and per-event cumulative M_0 (right axis) for slow (left panel) and fast (right panel) slip events. Each vertical strip corresponds to one slip event, with AE plotted at their real recording time (ms) relative to the first AE of that event; alternating shading distinguishes consecutive events, and the 2-ms scale bar (top left of each panel) indicates the common time base.

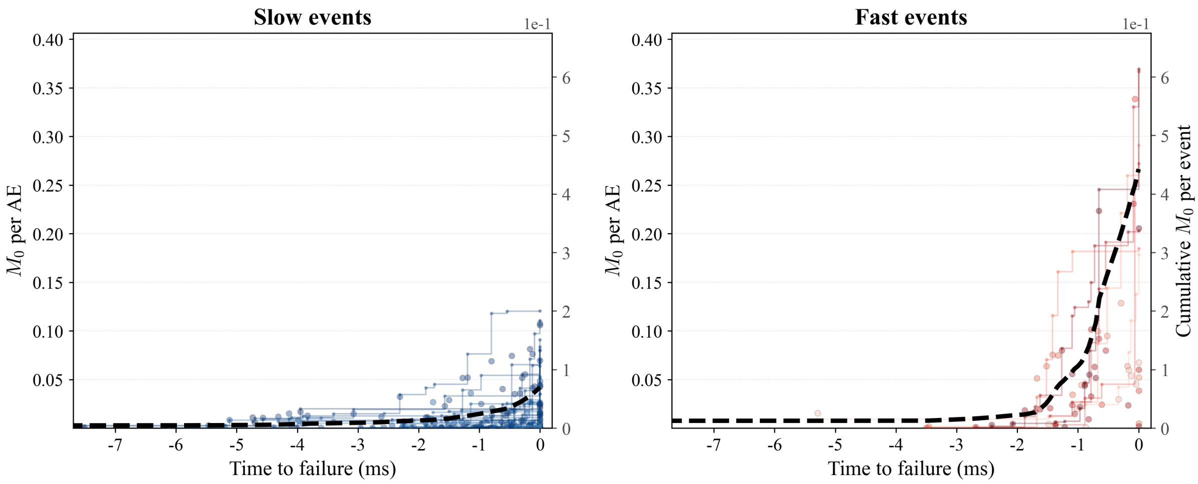

Supplementary Figure 19: Acoustic emission evolution relative to failure across all experiments. M_0 of individual AE (left axis) and per-event cumulative M_0 (right axis) as a function of time to failure (ms; $t = 0$ corresponds to the final AE of each event) for slow (left panel) and fast (right panel) slip events. Colored circles and step lines show individual events; the black dashed line is the mean cumulative-M_0 trajectory obtained by linearly interpolating each event onto a common time grid and averaging across events. Slow events show a gradual, near-linear accumulation of seismic moment over several milliseconds preceding failure, consistent with the AE-swarm behavior described for slow slip, whereas fast events accumulate a comparable or larger cumulative M_0 within a shorter interval immediately before failure, reflecting the more efficient, clustered energy release characteristic of fast slip.